Pushing the characterization of exoplanet atmospheres down to temperate rocky planets in the era of JWST

Zieba, S.

5

A Hubble WFC3 infrared look at the transmission spectrum of the hot, inflated sub-Saturn KELT-11 b

Sebastian Zieba, Knicole D. Colón, Luis Welbanks, Laura Kreidberg, Kevin B. Stevenson, Dana R. Louie, Daniel Angerhausen, Thomas Barclay, Thomas Beatty, Jonathan J. Fortney, David J. James, Michael R. Line, Eric D. Lopez, Nikku Madhusudhan, Avi Mandell, Erin May, Joseph E. Rodriguez, and Keivan G. Stassun
In Preparation, 2024.

Abstract

The high equilibrium temperature (1703K), low density (nine times less than Saturn), and bright host star (V = 8 mag) make KELT-11 b a perfect target for atmospheric characterization via transmission spectroscopy. Here, we present a new transmission spectrum for this hot, inflated sub-Saturn taken by the *Hubble Space Telescope* (*HST*) using its Wide Field Camera 3 (WFC3). We analyze unpublished *HST*/WFC3 G102 (0.8 – 1.1 µm) spectroscopic grism data collected in December 2020 and also perform a reanalysis of the *HST*/WFC3 G141 (1.1 – 1.7 µm) data collected in April 2018, previously published in Colón et al. (2020). We perform a thorough study of the systematic effects observed in the dataset and lay out how different model assumptions change the final transmission spectrum. We find that the commonly used `divide-white` technique can lead to systematic bias in the transmission spectrum in cases where the systematic noise varies with wavelength (e.g. Sun-like stars). The unusual transmission shape in the G141 grism seen by Colón et al. (2020) is most likely caused by the choice of the `divide-white` technique. Our G141 spectrum shows smaller transit depths at the red edge of the detector, similar to other hot, inflated sub-Saturns previously studied with WFC3 G141, like WASP-39 b and WASP-107 b. The transit depth of our G102 spectrum decreases toward shorter wavelengths, which is indicative of faculae on the stellar photosphere contaminating our spectrum.

5.1 Introduction

KELT-11 b was detected in photometric ground-based and radial velocity data (Pepper et al. 2017) and later also observed by the *Spitzer Space Telescope* at 3.6 µm (Beatty et al. 2017). The planet orbits a bright (V = 8.04 mag, H = 6.25 mag, Ks = 6.12 mag), evolved subgiant (KELT-11, HD 93396) (Pepper et al. 2017). With an exceptionally low planetary density of just 0.08 ± 0.02 g/cm^3 (compare to $\rho_{\mathrm{Saturn}} = 0.687$ g/cm^3), the planet is part of the population of hot inflated Saturns (Colón et al. 2020) (see Fig. 5.1 and Table 5.1). The planet also has a short orbital period of 4.7361 days (Beatty et al. 2017), leading to a high equilibrium temperature of approximately 1700 K (following Koll et al. 2019b, assuming A_B = 0 and uniform redistribution). Taken together, the planet's low surface gravity, high equilibrium temperature, and bright host star make KELT-11 b an excellent target for atmospheric follow-up using transmission spectroscopy.

Another member of the group of hot inflated Saturns is WASP-39 b (Faedi et al. 2011), which was recently extensively studied as part of *JWST*'s Early Release Science (ERS) program (JWST Transiting Exoplanet Community Early Release Science Team et al. 2023; Ahrer et al. 2023; Alderson et al. 2023; Rustamkulov et al. 2023; Feinstein et al. 2023; Tsai et al. 2023). The planet was found to have a strong CO_2 absorption feature, expected in chemical equilibrium for ∼10x solar composition (Mollière et al. 2015), which is comparable to Saturn's metallicity (Atreya et al. 2022). This measurement for WASP-39 b is therefore in agreement with the metallicity-mass trend observed for the solar system gas giants, which shows that a planet's mass is indirectly proportional to its atmospheric metallicity (Kreidberg et al. 2014b; Welbanks et al. 2019). For KELT-11 b, however, the *HST*'s Wide Field Camera 3 (WFC3) G141 observations published in Colón et al. (2020) showed a different picture of the planet: the observed water abundance of the planet was determined to be orders of magnitude lower than previously expected from planet formation models. Depending on the chosen model, the data also showed hints of carbon- and oxygen-bearing species (HCN, TiO, and AlO) (Colón et al. 2020). The presence of a lower-than-anticipated water abundance in the sub-Saturn KELT-11 b, from the perspective of planet formation, is intriguing. Models predict that the atmospheric metal enrichment for sub-Saturns, ranges from 10 – 100 times the solar composition, regardless of whether these planets form interior or exterior to the water ice line (Fortney et al. 2013; Mordasini et al. 2016). Interior structure models, derived from the observed masses and radii of gas giant exoplanets, also indicate a metal enrichment of approximately 10 times the solar composition for planets within the sub-Saturn mass range (Thorngren et al. 2016). However, Colón et al. (2020) atmospheric retrievals for KELT-11 b resulted in a sub-solar water abundance (0.01 – 0.1 times solar), significantly lower than the anticipated values by several orders of magnitude.

In this paper, we reanalyze the *HST*/WFC3 G141 observations originally published in Colón et al. (2020) and present a planetary transmission spectrum, which is inconsistent with the previously published transmission spectrum. We also analyze new observations taken by the G102 grism. In Section 5.2 and 5.3, we describe the observations, data reduction, and light curve fitting. We discuss our G141 and

G102 transmission spectra in Section 5.4.1 and 5.4.3. In Section 5.4.2 we compare our G141 spectrum with some other planets with similar properties. Finally, we summarize our findings in Section 5.5.

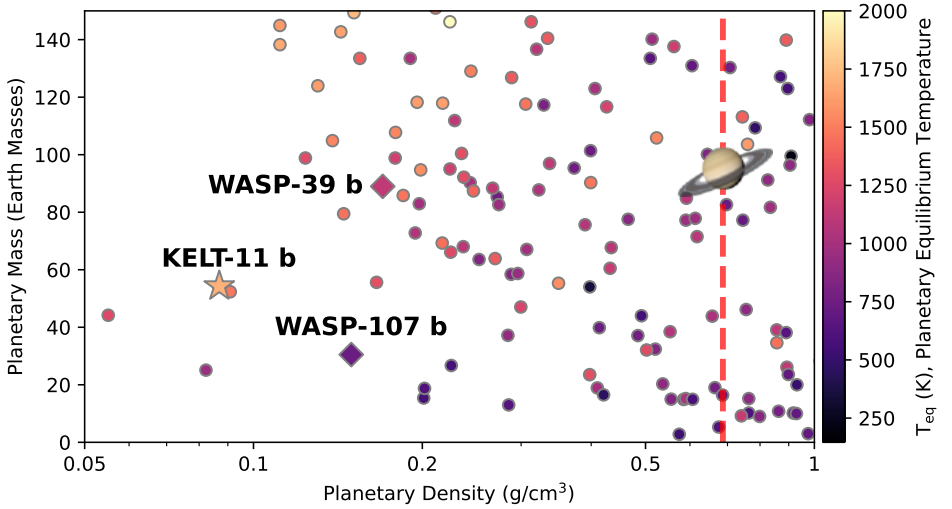

Figure 5.1: Exoplanets with low densities, highlighting KELT-11 b (star symbol), the *JWST* ERS target WASP-39 b (diamond symbol), and WASP-107 b (diamond symbol). These three planets have some of the lowest densities while having (sub-)Saturn-like masses. We only show planets with bright host stars (K_s < 12 mag) and well-characterized planetary masses and radii ($> 5\sigma$). A list of properties for the highlighted planets is listed in Table 5.1. Data were taken from the NASA Exoplanet Archive in December 2023.

5.2 Observations and Data Reduction

We observed two transits of KELT-11b with *HST*'s Wide Field Camera 3 (WFC3) as part of the General Observer (GO) Programs 15255 (Colon 2017) and 15926 (Colon et al. 2019) (see Table 5.2 for a summary of the observations). The first transit was taken with the G141 grism (1.1 – 1.7 µm) on 2018 April 18 and originally published in Colón et al. (2020). Here, we conduct a reanalysis of this data. The second transit was taken with the G102 grism (0.8 – 1.1 µm) on 2020 December 28. Both observations consisted of 9 consecutive *HST* orbits and were taken in round-trip spatial scan mode, where we alternated between forward and reverse scans (McCullough & MacKenty 2012; Deming et al. 2013). With this setup, the stellar light is spread over more pixels by slewing the telescope in the cross-dispersion direction. This effectively increases the exposure time and duty cycle of the observations without reaching saturation, but leads to a constant offset between forward and reverse scans, which we will correct for in the fitting stage.

Both observations used an identical observational setup: the data were taken

Table 5.1: A selection of planets, which are part of the hot, inflated (sub-)Saturn population. References: KELT-11 b: Beatty et al. (2017); WASP-39 b: Faedi et al. (2011); WASP-107 b: Anderson et al. (2017); Piaulet et al. (2021)

Planet	$R_p(R_J)$	$M_p(M_J)$	ρ_p (g/cm^3)	$P_{\rm orb}$ (d)	$T_{\rm eq}$ (K)	$R_*(R_s)$	[Fe/H]$_*$ (dex)
KELT-11 b	1.35 ± 0.10	0.171 ± 0.015	0.092 ± 0.022	4.74	1703	2.7	0.17 ± 0.07
WASP-39 b	1.27 ± 0.04	0.280 ± 0.030	0.182 ± 0.026	4.06	1118	0.9	0.01 ± 0.09
WASP-107 b	0.94 ± 0.02	0.096 ± 0.005	0.154 ± 0.013	5.72	733	0.7	0.02 ± 0.10
Saturn	0.83	0.30	0.687				

Table 5.2: Summary of the two *HST*/WFC3 observations analyzed in this work, with $N_{\rm orb}$ being the number of orbits and $N_{\rm exp}$ the number of spectroscopic exposures in each program.

Instrument	GO ID	Date (UT)	$N_{\rm orb}$	$N_{\rm exp}$
HST/WFC3/G141	15255	2018-04-18	9	234
HST/WFC3/G102	15926	2020-12-28	9	261

with the 512x512 subarray (SQ512SUB) and had a scan rate of 0.96 arcsec/sec (7.4 pixels/sec). We used the SPARS25 read-out mode with NSAMP = 4, resulting in an exposure time of 46.7 seconds for both visits. This led to a scan length of 53.1 arcsec or 395 pixels. We reached a maximum photoelectron count per pixel of approximately 2.9×10^4 electrons per second for G102 and 4.8×10^4 electrons per second for G141, which is below the non-linear regime of the WFC3 detector for both of the observations (Hilbert 2008). We started every *HST* orbit with an undispersed "direct image" of the star using the WFC3 F130N narrow-band filter, which we used to determine the position of the spectroscopic trace (see Fig. 5.2). The direct images were then typically followed by 26 (31) spectroscopic exposures per *HST* orbit, leading to 234 (261) 2D spectra in total for the G102 (G141) observations.

We accessed and downloaded the calibrated intermediate IR multiaccum image (IMA) files[1] which were produced by the `calwf3` pipeline version 3.6.2 from MAST[2]. These files have calibrations like dark subtraction, linearity correction, and flat fielding applied to each individual readout of the exposure. We then reduced this data with the end-to-end open-source pipeline `PACMAN`[3] (Zieba & Kreidberg 2022) which is based on the procedure described in previous works (see e.g., Kreidberg et al. 2014a,b, 2015, 2018a). By observing the star with the spatial scanning technique, each exposure consists of a number of non-destructive reads, which are also called "up-the-ramp samples" (see Fig. 5.2). We treat each of them as an independent subexposure and start by masking bad pixels, which were flagged by the `calwf3` with a data quality flag of either DQ = 4 or 512[4]. Next, we calculated the difference between consecutive non-destructive reads and subtracted the background. We determined the background flux of each difference frame by computing the median flux of the pixels where the stellar light did not fall on the detector. The background flux per pixel was $\sim$33 e^-/sec during the G102 observations increasing at the end of each orbit and $\sim$58 e^-/sec during the G141 observations being highest at the beginning of each orbit (see Fig. 5.3). We then optimally extract each of the background subtracted difference images by following the algorithm presented in Horne (1986). For each of the subexposures, we chose an extraction window that corresponded to $\pm$20 pixels relative to the upper and lower edges of the spectrum[5]. We then summed up the spectra for all the differenced images to get the final 1D spectrum for each exposure (see Fig. 5.4). Finally, we performed a wavelength calibration on these 1D spectra by cross-correlating them with a reference spectrum. The reference spectrum consisted of the product of the bandpass of the respective grism and a smoothed stellar spectrum following Deming et al. (2013). The chosen stellar spectrum was an ATLAS9 stellar atmosphere model by Castelli & Kurucz (Castelli & Kurucz 2003), which was the closest one to the published stellar parameters in Beatty et al. (2017), i.e.,

[1] for more information on the "ima" data products see the WFC3 Data Handbook: `https://hst-docs.stsci.edu/wfc3dhb/chapter-2-wfc3-data-structure/2-1-types-of-wfc3-files`

[2] `https://mast.stsci.edu/search/hst`

[3] for `PACMAN`'s documentations see: `https://pacmandocs.readthedocs.io/en/latest/`

[4] for an explanation of the various `calwf3` quality flags see `https://wfc3tools.readthedocs.io/en/latest/wfc3tools/calwf3.html\#data-quality-initialization-dqicorr`

[5] for more details see `https://pacmandocs.readthedocs.io/en/latest/pcf.html\#window`

the stellar model with $T_{\rm eff}$ = 5250K, log(g) = 3.5 and [M/H] = +0.2[6].

5.3 Light Curve Analysis

5.3.1 *HST*/WFC3 White Light Transit

We generated white (i.e., broadband) light curves by summing the flux in the 1D spectra (see Fig. 5.4) for each exposure. The resulting light curves can be seen in Figure 5.3. They exhibit systematics that are typical for *HST*/WFC3 observations like the offset caused by the "upstream/downstream" effect or a ramp-like trend in each *HST* orbit. The latter is caused by charge-trapping in the WFC3 detector (Zhou et al. 2017). We discard the first orbit of the WFC3 observations because they have stronger ramp amplitudes compared to the following orbits, which is common practice (see e.g., Deming et al. 2013; Kreidberg et al. 2014a; Wakeford et al. 2017). We also remove the first exposure of each *HST* orbit due to their strong systematics.

HST/WFC3 observations also typically show visit-long drifts in the baseline level which are typically fitted by low-order time-dependent polynomials, i.e., linear or quadratic trends. Like in Guo et al. (2020), we also explore exponential and logarithmic visit-long trends to describe this drift in flux.

Our final fitting model $F(t)$ consists out of a `batman` (Kreidberg 2015) transit model $F_{\rm transit}(t)$, the orbit-long systematics $F_{\rm sys,o}(t)$, and the visit-long systematics $F_{\rm sys,v}(t)$:

$$F(t) = F_{\rm transit}(t) F_{\rm sys,o}(t) F_{\rm sys,v}(t). \tag{5.1}$$

As in previous work, we model the ramp-like trends in each *HST* orbit with an exponential function, which is commonly also called "model-ramp":

$$F_{\rm sys,o}(t) = 1 - \exp(-r_1 t_{\rm o} - r_2 - D(t)), \tag{5.2}$$

where r_1 describes the rate of the exponential function and r_2 its amplitude. The delay function, $D(t)$, has the value of r_3 for the first orbit and is 0 otherwise. This is an optional parameter, which might be used if the first orbit exhibits a stronger orbit-long ramp than the following orbits (in this case, r_3 would have a negative value). The time elapsed from the first exposure in each orbit is described by $t_{\rm o}$.

We compared the following visit-long trends:

$$F_{\rm sys,v}(t) = \begin{cases} c\,S(t) + v_1 t_{\rm v}, & \text{linear} \\ c\,S(t) + v_1 t_{\rm v} + v_2 t_{\rm v}^2, & \text{quadratic} \\ c\,S(t) + \exp(-e_1\, t_{\rm v})\, e_2, & \text{exponent.} \\ c\,S(t) + \log(t_{\rm v} + 1/l_1)\, l_2, & \text{logarith.} \end{cases} \tag{5.3}$$

with $t_{\rm v}$ being the time elapsed since the first exposure in a visit and c is a normalization constant. The scale function, $S(t)$, accounts for the offset caused by

[6] we accessed the Castelli & Kurucz stellar spectrum from MAST `https://archive.stsci.edu/hlsps/reference-atlases/cdbs/grid/ck04models/`

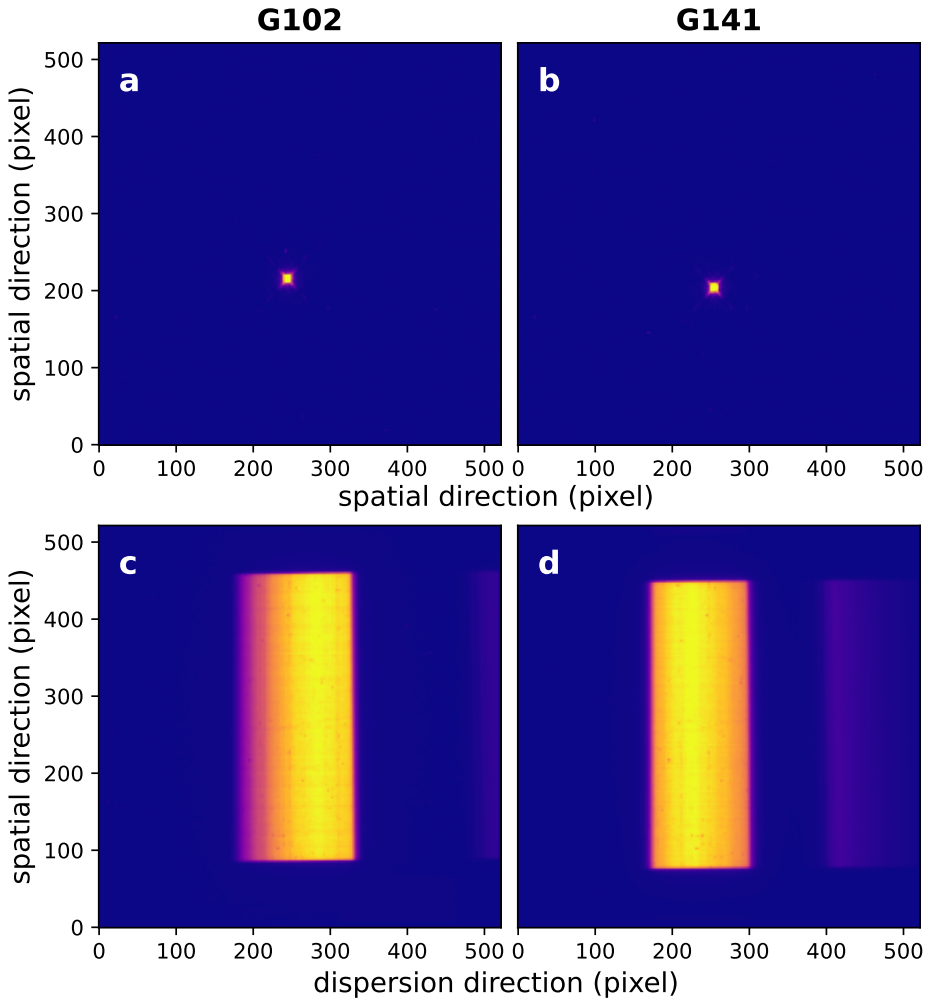

Figure 5.2: Examples of calibrated intermediate IR multiaccum image (IMA) files using the 512x512 subarray (SQ512SUB) on *HST*/WFC3. The top panels show the undispersed "direct images" of KELT-11 taken with the WFC3 F130N narrow-band filter for the G102 (panel a) and G141 (panel b) observations. The bottom panels c and d show first-order 2D spectra for the last up-the-ramp sample (i.e., the last non-destructive read) for a randomly chosen exposure in each observation. The faint second-order spectra (which are not used in this work) can be seen on the right side of the subarray.

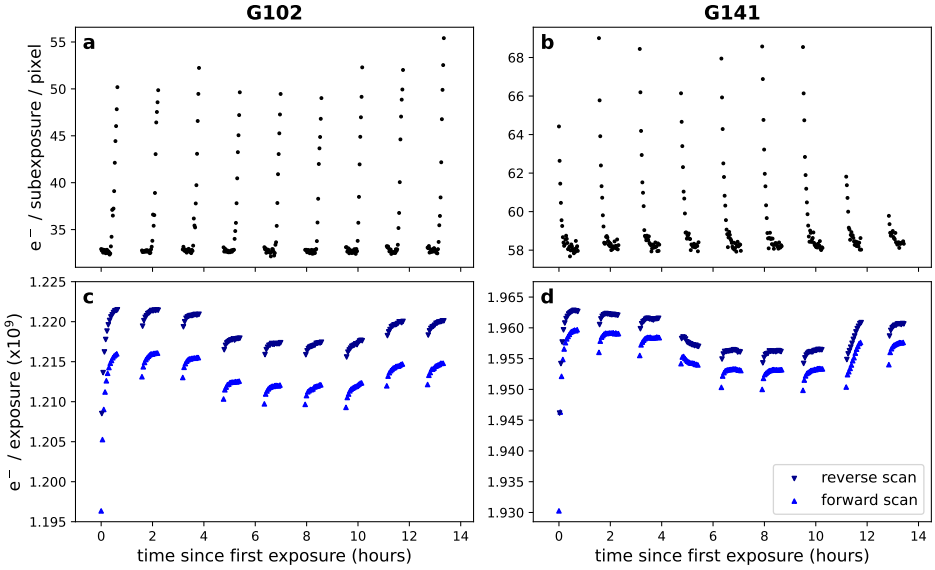

Figure 5.3: Top row: background flux of each up-the-ramp sample (subexposure) per pixel as a function of time. Bottom row: raw white light curves after performing the data reduction described in Section 5.2. The offset caused by the "upstream/downstream" effect can be clearly seen by observing in the round-trip spatial scan mode. This is caused by the total integration time effectively sightly increasing when the scan is "downstream" ("reverse scanning") because the star will be moved on the detector in the same direction as the readout (McCullough & MacKenty 2012).

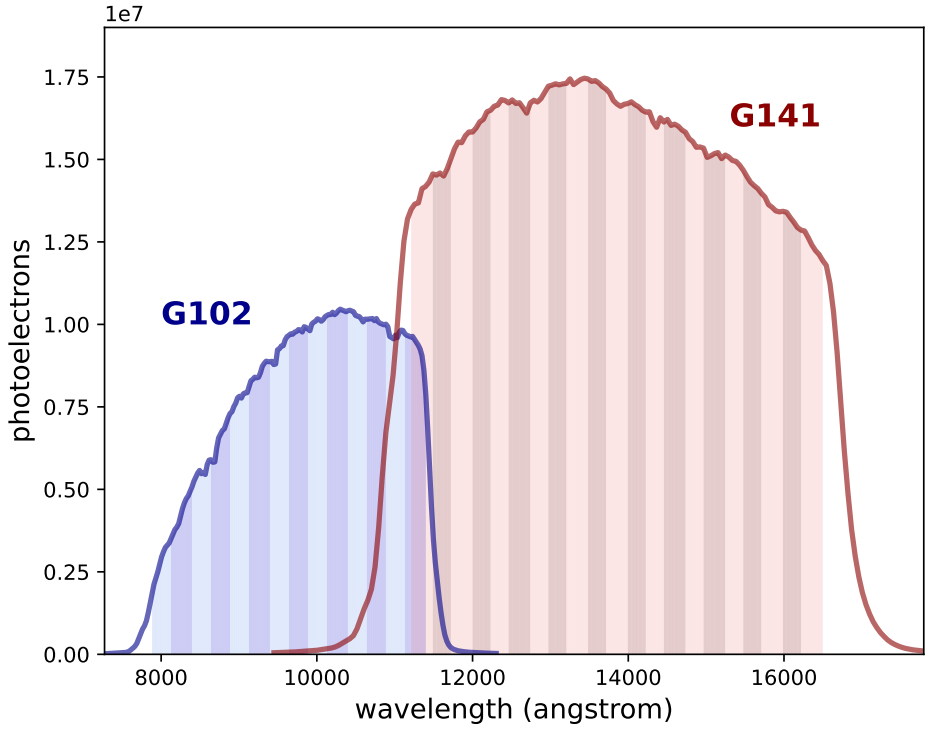

Figure 5.4: Wavelength calibrated 1D spectra of KELT-11 for a random exposure taken during both observations. The alternating colors under the curves depict the chosen binning for the spectroscopic light curves, which was chosen to be 0.025 µm for both observations.

the "upstream/downstream" effect and is 1 for exposures taken with a forward scan direction and s for reverse scans. For our observations, this offset is ∼0.4% for G102 and ∼0.2% for the G141 data. Finally, v_1, v_2, e_1, e_2, l_1, and l_2 are free parameters for the respective trends, which describe the shape of the visit-long systematic.

For the transit model, the free parameters were the transit midpoint time t_0, the planet-to-star radius ratio R_p/R_s, the ratio of semimajor axis to stellar radius a/R_s, the orbital inclination i and the limb darkening. We fixed the orbital period of the planet $P_{\rm orb}$ to a literature value and used normal priors for a/R_s and i based on Beatty et al. (2017) (see Table 5.3). We also fixed the eccentricity to zero as previous studies found that the orbits were all consistent with a circular orbit (Beatty et al. 2017; Pepper et al. 2017; Colón et al. 2020). We tested both a linear limb darkening and a two-parameter limb darkening following the parameterization described in Kipping (2013). The second orbit in a visit is known to sometimes exhibit a stronger orbit-long ramp than the following ones. Due to that, we also test if our fit improves when we use the delay function $D(t)$ on that orbit or if we get a better fit by removing the orbit altogether. We also fit for an uncertainty-multiplier factor $\sigma_{\rm multi}$, which scales the error bars of our data, so that the model reaches a reduced chi-squared of one ($\chi^2_{\rm red.} = 1$), which accounts for any additional not-photon-limited noise in the observations and ensures that we are not underestimating the uncertainties of our fitted parameters.

Table 5.3: Adopted literature values from Beatty et al. (2017) for the white light curve fits in this work.

Parameter	Value
$P_{\rm orb}$ (days)	4.7361
a/R_s	4.98 ± 0.05
i ($^\circ$)	85.3 ± 0.2

We determine the best-fit model by minimizing the Bayesian information criterion (BIC; Schwarz 1978) where we apply the definition that a ΔBIC value greater than 10 shows strong evidence against a given model (Kass & Raftery 1995). A table with all explored models for the G102 and G141 observations and values like the BIC or χ^2 can be found in the Appendix (Table 5.7 and 5.8). We use the dynamic nested sampling approach (Skilling 2004, 2006; Higson et al. 2019) implemented in the open-source python package `dynesty` (Speagle 2020; Koposov et al. 2023b) to estimate our free parameters and their uncertainties (details in Appendix 5.A). For both datasets, we find that the white light curve is best fitted by a quadratic limb darkening law. The best fitting visit long trend for the G102 data is a quadratic function and for G141 an exponential function. We furthermore find that removing the first two orbits for the G102 observations and orbit number one and five for G141 significantly improves the fits. The best white light curve fits for both datasets are shown in Figure 5.5. Our final residuals display

Table 5.4: Free parameters from the *HST*/WFC3 G102 and G141 white light curves. The values correspond to the median of the posterior distribution of the white light curve fits and their 16th and 84th percentiles.

Parameter	Value
G102	
t_0 ($\mathrm{BJD_{TBD}}$)	2459212.1374 ± 0.0018
a/R_s	5.00 ± 0.05
i ($^\circ$)	$85.27^{+0.20}_{-0.19}$
R_p/R_s	0.0452 ± 0.0003
$q1$	$0.24^{+0.08}_{-0.07}$
$q2$	$0.05^{+0.09}_{-0.04}$
$u1$ (derived)	$0.05^{+0.07}_{-0.04}$
$u2$ (derived)	$0.44^{+0.10}_{-0.14}$
G141	
t_0 ($\mathrm{BJD_{TBD}}$)	$2458227.01495 \pm 0.00008$
a/R_s	4.95 ± 0.02
i ($^\circ$)	$85.17^{+0.16}_{-0.14}$
R_p/R_s	0.04630 ± 0.00009
$q1$	0.167 ± 0.017
$q2$	0.11 ± 0.06
$u1$ (derived)	$0.09^{+0.05}_{-0.04}$
$u2$ (derived)	0.32 ± 0.06

a low amount of scatter. We measure a root-mean-squared (rms) variability of 71.6 ppm for G102 and 37.6 ppm for G141. This is 2.5× and 1.6× the expected Poisson noise. Our G141 residuals show considerably less scatter than the 65ppm (3× poission) published in Colón et al. (2020). This is mostly due to removing the fifth orbit which exhibits more scatter and determining that an exponential trend is approximating the visit long systematics better than the quadratic trend used in Colón et al. (2020) (see Tab. 5.8 for all models fitted to the G141 white light curve). Our final results for the white light curve fits for both grisms are listed in Table 5.4.

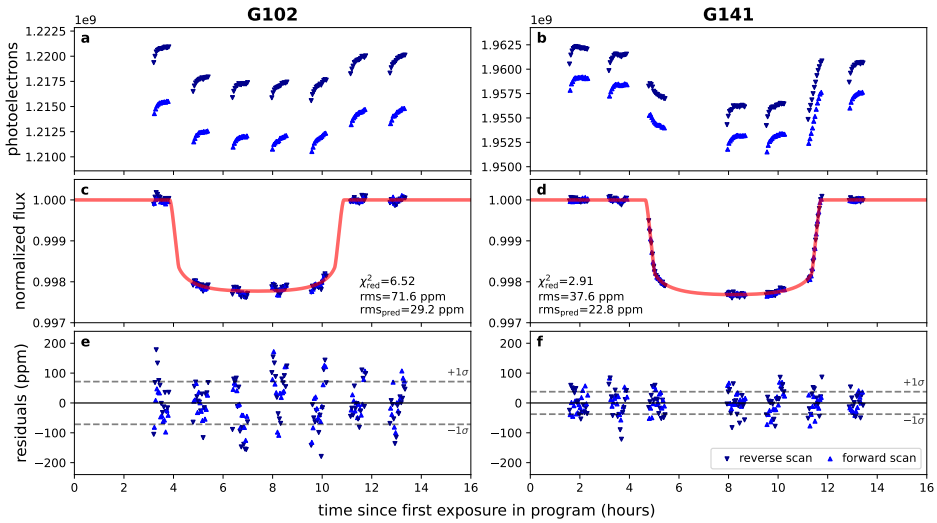

Figure 5.5: Best white light curve fits for the G102 and G141 observations. Top row: Raw white light curve. Orbit 1 and 2 were removed for the G102 data and orbit 1 and 5 for the G141 observations. Middle row: Best white light curve fit with the visit and orbit long trends removed. The red line shows the best fitting `batman` model. Lower row: The residuals from the best fit. The standard deviation of the residuals is shown by dashed lines.

5.3.2 *HST*/WFC3 Spectroscopic Transit

We create spectroscopic light curves by binning each of the observations. The wavelengths we considered are 0.79 – 1.14 µm for the G102 grism and 1.125 – 1.650 µm for the G141 grism. We chose a bin width of 0.025 µm for both datasets, leading to 14 and 21 spectroscopic bins for the G102 and G141 data, respectively. We fit the visit long systematics of each spectroscopic light curve with the best white light curve model, that is, a quadratic trend for G102 and an exponential trend in time for G141. We furthermore fit each light curve with a transit model with a quadratic limb darkening law (u_1, u_2) and exponential ramp for each orbit. We fix the transit time t_0 to the best-fitting values listed in Table 5.4 for each

of the grisms. We also fixed $P_{\rm orb}$, a/R_s, and i to the values reported in (Beatty et al. 2017) (see Table 5.3). Each spectroscopic light curve fit therefore had 10 free parameters: R_p/R_s, u_1, u_2, c, s, r_1, r_2, $\sigma_{\rm multi}$ and two visit long parameters (e_1 and e_2 for G102; v_1 and v_2 for G141). We used the dynamic nested sampling code `dynesty` to sample the posteriors of each of these parameters and used the same setup as for the white light curve fits (see Appendix 5.A).

In Figure 5.14 and 5.15, we show the individual spectroscopic light curve fits. Figure 5.6 shows the transmission spectrum of KELT-11 b after fitting our models to each spectroscopic light curve (the data can be found in Table 5.5 and 5.6). We find that the shape of our G141 spectrum significantly deviates from the transmission spectrum published in Colón et al. (2020) (see Figure 5.7). In particular, our G141 spectrum shows decreasing absorption at longer wavelengths. The Colón et al. (2020) spectrum was comparatively flat between 1.40 and 1.65µm. The final model chosen in Colón et al. (2020) used the `divide-white` technique, which assumes that the observed systematics are not wavelength-dependent but have the same shape across the detector (Stevenson et al. 2014a; Kreidberg et al. 2014a). For that, each spectroscopic light curve is fit by the astrophysical model (in our case a transit) multiplied by the scaled systematics of the best-fitting white light curve. For a more detailed discussion of the `divide-white` technique, see Section 5.4.1.

We also search for correlated noise in the residuals of our spectroscopic light curve fits. For that, we calculate the rms of the residuals for bins of different sizes. The rms of our light curve residuals decrease with increasing bin size and follow the $1/\sqrt{N}$ line, which is expected if the residuals are dominated by Poisson noise. This suggests that our residuals are uncorrelated in time. See Figure 5.17 for the Allan deviation plots for each of the spectroscopic light curve fits. We list the various properties of our spectroscopic light curve fits like rms and χ^2 in Table 5.9. By calculating the ratio between our achieved residual rms and the predicted rms in the case of the presence of only Poisson noise, we determine that we range from 3% to 34% above the photon limit for the G102 data and 2% below to 51% above it for G141.

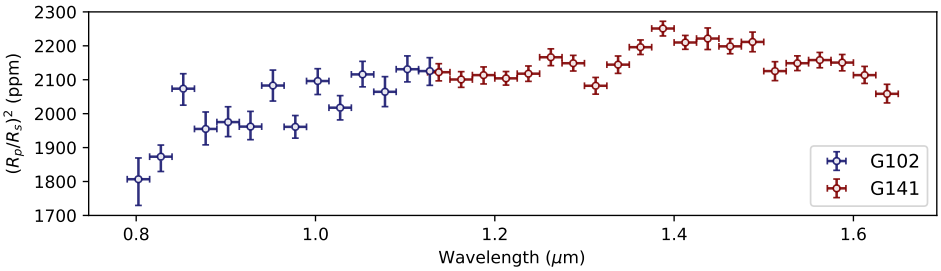

Figure 5.6: The full *HST*/WFC3 transmission spectrum of KELT-11 b using the G102 (midnight blue bins) and G141 (maroon bins) grisms. The data for this figure is listed in Tabel 5.5 and 5.6.

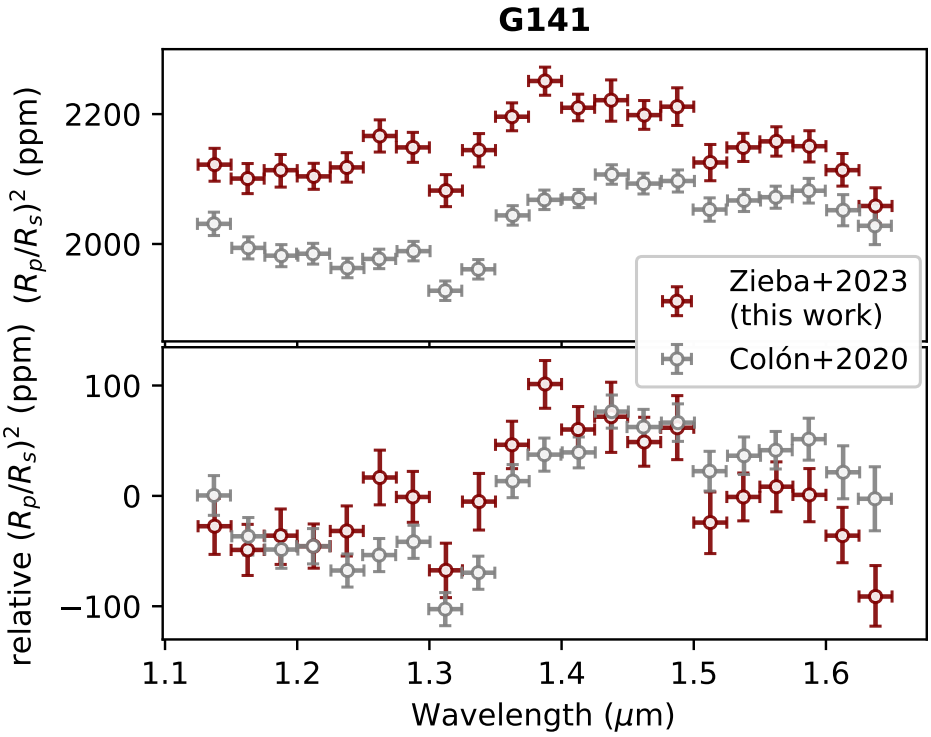

Figure 5.7: Comparison of the G141 transmission spectrum of KELT-11 b presented in this work (maroon bins) compared to the spectrum published in Colón et al. (2020) (gray bins). In the lower panel, we subtracted the mean transit depth from each transmission spectrum.

Table 5.5: Planet-to-star ratio (R_p/R_s) and transit depth $(R_p/R_s)^2$ in ppm for each spectroscopic light curve fit using the G102 grism data. Each of the bins has a half width of 0.0125 µm. So e.g., the 1.1275 µm bin covers the wavelengths 1.115 µm to 1.140 µm. The R_p/R_s values listed in the Table correspond to the median of the posterior distribution and the errorbars to the 14th and 86th percentiles.

$\lambda_{\rm mid}$(µm)	R_p/R_s	$(R_p/R_s)^2$ (ppm)
0.8025	$0.04251^{+0.00074}_{-0.00091}$	1807^{+63}_{-77}
0.8275	$0.04328^{+0.00040}_{-0.00050}$	1873^{+34}_{-44}
0.8525	$0.04554^{+0.00048}_{-0.00053}$	2074^{+44}_{-49}
0.8775	$0.04422^{+0.00057}_{-0.00053}$	1955^{+50}_{-47}
0.9025	$0.04444^{+0.00051}_{-0.00048}$	1975^{+45}_{-43}
0.9275	$0.04429^{+0.00051}_{-0.00044}$	1962^{+45}_{-39}
0.9525	$0.04564^{+0.00050}_{-0.00050}$	2083^{+46}_{-46}
0.9775	$0.04428^{+0.00038}_{-0.00038}$	1961^{+33}_{-33}
1.0025	$0.04578^{+0.00040}_{-0.00043}$	2096^{+36}_{-40}
1.0275	$0.04492^{+0.00040}_{-0.00040}$	2018^{+36}_{-36}
1.0525	$0.04600^{+0.00042}_{-0.00040}$	2116^{+38}_{-37}
1.0775	$0.04544^{+0.00049}_{-0.00048}$	2064^{+45}_{-44}
1.1025	$0.04616^{+0.00043}_{-0.00041}$	2131^{+39}_{-37}
1.1275	$0.04610^{+0.00043}_{-0.00046}$	2126^{+40}_{-42}

Table 5.6: Same as Table 5.5 but for the spectroscopic light curve fits to the G141 grism data.

$\lambda_{\rm mid}$ (µm)	R_p/R_s	$(R_p/R_s)^2$ (ppm)
1.1375	$0.04607^{+0.00027}_{-0.00028}$	2122^{+25}_{-26}
1.1625	$0.04583^{+0.00025}_{-0.00025}$	2101^{+23}_{-23}
1.1875	$0.04597^{+0.00026}_{-0.00028}$	2114^{+24}_{-26}
1.2125	$0.04587^{+0.00022}_{-0.00022}$	2104^{+20}_{-20}
1.2375	$0.04602^{+0.00025}_{-0.00025}$	2118^{+23}_{-23}
1.2625	$0.04654^{+0.00027}_{-0.00027}$	2166^{+25}_{-25}
1.2875	$0.04635^{+0.00025}_{-0.00025}$	2149^{+23}_{-23}
1.3125	$0.04563^{+0.00027}_{-0.00027}$	2082^{+25}_{-25}
1.3375	$0.04631^{+0.00028}_{-0.00028}$	2145^{+26}_{-26}
1.3625	$0.04686^{+0.00023}_{-0.00023}$	2196^{+21}_{-22}
1.3875	$0.04744^{+0.00022}_{-0.00023}$	2251^{+21}_{-22}
1.4125	$0.04701^{+0.00022}_{-0.00021}$	2210^{+21}_{-20}
1.4375	$0.04713^{+0.00033}_{-0.00034}$	2221^{+31}_{-32}
1.4625	$0.04689^{+0.00024}_{-0.00023}$	2198^{+22}_{-22}
1.4875	$0.04703^{+0.00031}_{-0.00031}$	2211^{+29}_{-29}
1.5125	$0.04610^{+0.00030}_{-0.0003}$	2125^{+28}_{-28}
1.5375	$0.04635^{+0.00023}_{-0.00023}$	2149^{+22}_{-22}
1.5625	$0.04645^{+0.00024}_{-0.00024}$	2158^{+23}_{-23}
1.5875	$0.04637^{+0.00026}_{-0.00026}$	2151^{+24}_{-24}
1.6125	$0.04597^{+0.00028}_{-0.00027}$	2114^{+26}_{-25}
1.6375	$0.04537^{+0.00031}_{-0.00030}$	2058^{+28}_{-27}

5.4 Discussion

5.4.1 Systematic bias from divide-white fitting technique

In Figure 5.7 we compare our reanalyzed G141 transmission spectrum of KELT-11 b with the one previously published in Colón et al. (2020). Notably, our spectrum reveals a distinctive "water bump" around 1.4 µm, a characteristic feature successfully identified in the atmospheres of numerous exoplanets using *HST*/WFC3 G141 (e.g., Deming et al. 2013; Huitson et al. 2013; Fraine et al. 2014; Kreidberg et al. 2014b; Evans et al. 2016). The initial shape of the G141 transmission spectrum, characterized by an unusually flat profile at the red edge of the detector, suggested the presence of another absorber at longer wavelengths, potentially HCN (we refer to Figure 16 in Colón et al. 2020). In Figure 5.16, we demonstrate that the shape of our spectrum remains consistent across different model assumptions (like the choice of limb darkening law or the functional form of the visit-long systematic trend), further reinforcing the robustness of our findings. We also performed a `divide-white` fit to the G141 data in this work and were able to recreate the transmission spectrum published in Colón et al. (2020). In Figure 5.8, we show that the systematic parameters in the spectrum are not constant but reveal substantial variations across the detector. Consequently, we conclude that employing the `divide-white` approach is unsuitable for this dataset.

Kreidberg et al. (2015) noted that the `divide-white` technique might not always be appropriate because the systematics observed for the WFC3 detector are known to depend on the amount of illumination received (Berta et al. 2012; Swain et al. 2013). For our observations, the flux received by the different parts of the detector varies significantly: the spectroscopic bin corresponding to the most illuminated part of the detector receives 400% and 40% more flux than the least illuminated part for G102 and G141, respectively (see Fig. 5.4). The observations taken in Kreidberg et al. (2015) varied by 30%, which was reportedly enough to make `divide-white` an inadequate model choice. This might therefore be important to consider when working on *HST*/WFC3 near-infrared datasets of earlier type stars that exhibit significant brightness variations across wavelengths. Notably, in the two instances where the `divide-white` method substantially influenced the final spectrum shape, the stars in question were of earlier types: KELT-11 (this work) is a retired A star ($T_{\rm eff}$ = 5375K) and WASP-12 studied in Kreidberg et al. (2015) has a spectral type of G0V ($T_{\rm eff}$ = 6300K) (Bergfors et al. 2013; Hebb et al. 2009).

5.4.2 Comparison of G141 to other hot inflated sub-Saturns

Like in Colón et al. (2020), we compare our measured G141 spectrum with previously studied hot, inflated sub-Saturns like WASP-39 b (Wakeford et al. 2018) and WASP-107 b (Kreidberg et al. 2018b). Figure 5.9 shows the transmission spectra for KELT-11 b and the other two planets, showing a clear detection of water in the atmospheres for all three planets. The presence of water was also recently confirmed for WASP-39 b (e.g., JWST Transiting Exoplanet Community Early Release Science Team et al. 2023) and WASP-107 b (Dyrek et al. 2023), indicating

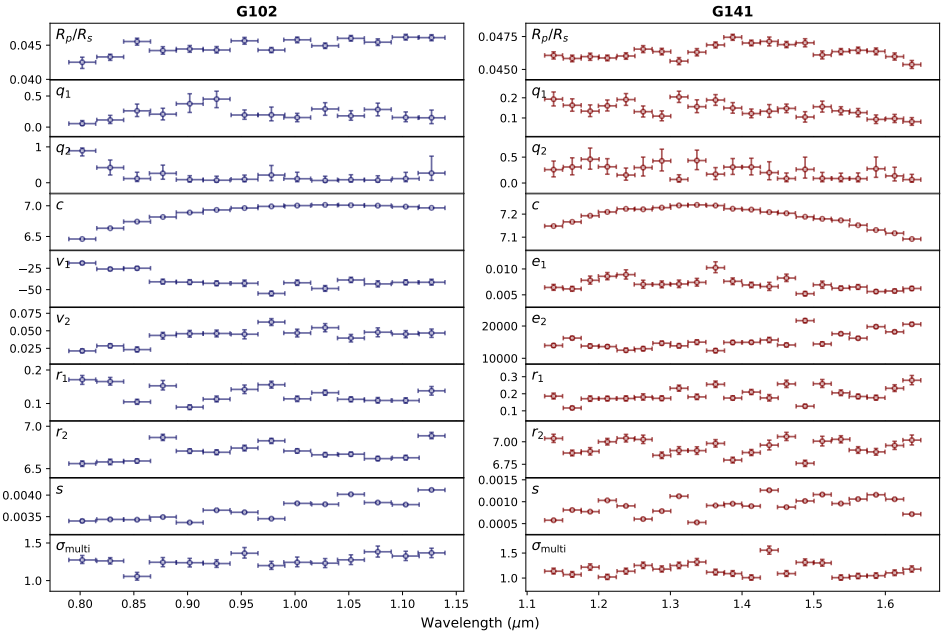

Figure 5.8: All free parameters as a function of wavelength for both datasets. The different parameters are described in Section 5.3.1.

a super-solar metallicity for both planets.

5.4.3 Shape of G102

Our G102 transmission spectrum of KELT-11 b (see Fig. 5.6) shows a decreasing transit depth with shorter wavelengths. This suggests hot faculae on the stellar photosphere, which are brighter areas on a star and are known to contaminate planetary transmission spectra (Pinhas et al. 2018). This has been observed for the mini-Neptune GJ 1214 b and the super-Earth GJ 1132 b. Their optical transmission spectra show lower transit depths compared to the infrared transits. Both of these planets orbit M-dwarfs (both approximately M4V stars Cloutier et al. 2021; Berta-Thompson et al. 2015), which are prone to exhibit photospheric heterogeneities like star spots and faculae, which influence the final transmission spectrum (Rackham et al. 2018). However, KELT-11 is not a late-type star but rather a retired A-type. Previous observations of the star also did not suggest significant stellar variability (see Colón et al. 2020, for a discussion of ground-based photometry). *TESS* observations taken in March 2019 and February 2023 also seem to not exhibit any periodic, coherent variability (Colón et al. 2020). The *CHEOPS* observations of KELT-11 b taken during its commissioning in March 2020 showed some variability, possibly due to granulation Benz et al. (2021). The amplitude of the signal is approximately 200 ppm on timescales between 30 minutes and 4 hours. We do not observe the same; on the contrary, our white light curves using

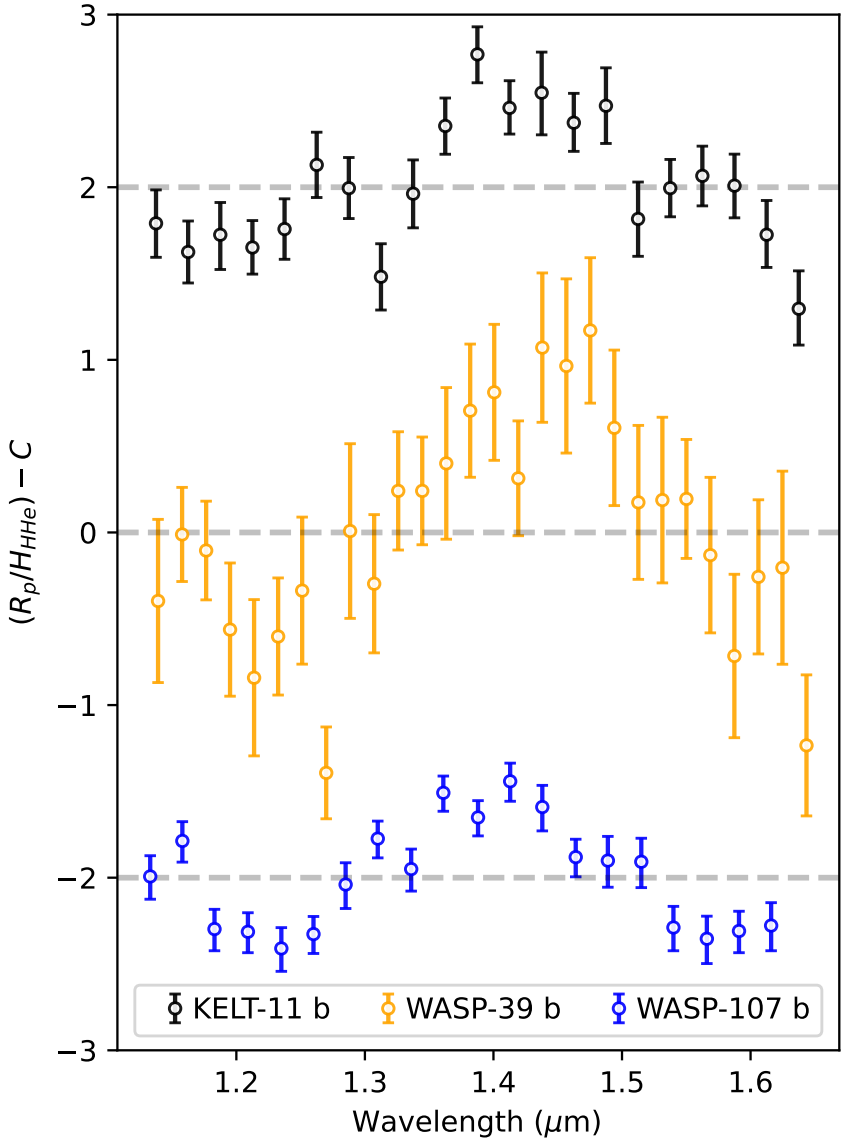

Figure 5.9: Comparison of the G141 transmission spectra of hot, inflated sub-Saturn planets following Colón et al. (2020). The KELT-11 b spectrum in the plot comes from this work, the WASP-39 b spectrum was published in Wakeford et al. (2018), and the WASP-107 b spectrum in Kreidberg et al. (2018b). We divided the planetary radius by the scale height ($H = \frac{k_B T_{\rm eq}}{\mu g}$), assuming a molecular weight of $\mu = 2.3$ g/mol (see Crossfield & Kreidberg 2017; Colón et al. 2020). To guide the eye, we show the mean for each planet as a horizontal line. All planets exhibit the well-known water absorption feature around 1.4 µm. We shifted the spectra by a constant C, for visualization purposes.

the G102 and G141 grism data seem stable and have high precision. Our Allan deviation plots (see Fig. 5.17) hint that we are not dominated by correlated noise from unaccounted instrumental systematics or stellar variability.

5.5 Summary

In this work, we have analyzed the *HST*/WFC3 data of KELT-11 b. Here, we summarize our main findings:

- The unusual shape of the *HST*/WFC3 G141 grism changes significantly when not using the `divide-white` technique, which assumes that the systematics have the same shape across the whole detector. We determine that `divide-white` is not adequate for this dataset because the systematic noise varies with wavelength. This should be taken into consideration for the analysis of other earlier type star WFC3 NIR data, where the stellar flux strongly varies with wavelength.
- Our G102 and G141 white light curves do not show any star spot crossing events or other forms of variability. We archive a precise white light curve with a root-mean-square (rms) of 71.6 ppm (for G102) and 37.6 ppm (for G141) for the residuals.
- Our G102 transmission spectrum of KELT-11 b reveals diminished transit depths at shorter wavelengths, likely attributed to contamination by faculae on the stellar photosphere during the time of observations. While this phenomenon has been previously observed in late-type stars like GJ 1132 and GJ 1214, it represents a novel observation for an earlier-type star like KELT-11.

In the future, using *JWST* to observe KELT-11 b presents a significant opportunity to probe its C/O ratio and provide crucial insights into the formation pathways of these inflated sub-Saturns. Additionally, KELT-11 b's high equilibrium temperature, low density, and bright host star make it an optimal target for atmospheric studies using *JWST*'s transmission spectroscopy, making it one of the most observable planets to date.

Acknowledgements

This research is based on observations made with the NASA/ESA Hubble Space Telescope obtained from the Space Telescope Science Institute, which is operated by the Association of Universities for Research in Astronomy, Inc., under NASA contract NAS 5–26555. These observations are associated with programs #15255 and #15926.

This research has made use of the NASA Exoplanet Archive, which is operated by the California Institute of Technology, under contract with the National Aeronautics and Space Administration under the Exoplanet Exploration Program.

We gratefully acknowledge the packages and tools that made this work possible: `batman` (Kreidberg 2015), `PACMAN` (Zieba & Kreidberg 2022), `dynesty` (Speagle 2020; Koposov et al. 2023b; Skilling 2004, 2006; Higson et al. 2019), `numpy` (Harris et al. 2020), `matplotlib` (Hunter 2007a), `astropy` (Astropy Collaboration et al. 2013, 2018, 2022).

Appendix

5.A Best fitting white light curve model

In order to find the two models that describe each of our datasets the best, we use the Bayesian Information Criterion (BIC; Schwarz 1978). The BIC is commonly used in exoplanet science for model selection. It measures how well a given model describes the data depending on the number of free parameters in the model and the amount of data points. It is defined as:

$$\mathrm{BIC} = -2\,\mathcal{L}_{\max} + k\,\ln(N), \tag{5.4}$$

where k is the number of free parameters in the model, N is the number of data points, and $\mathcal{L}_{\max}$ is the maximum likelihood given by:

$$\mathcal{L}_{\max} = -\frac{1}{2}\sum_i \left[\left(\frac{\mathrm{data}_i - \mathrm{model}_i}{\mathrm{err}_i} \right)^2 + \ln\left(2\pi\,\mathrm{err}_i^2\right) \right], \tag{5.5}$$

with data_i being the measured flux, err_i its uncertainty, and model_i the flux predicted by the model. From Equation 5.4 we can conclude that the preferred model is the one with the lower BIC value. It penalizes model complexity (high k) to avoid overfitting and penalizes models that do not fit the data well (low $\mathcal{L}_{\max}$).

For each of the models we tested, we used the dynamic nested sampling code `dynesty` (Speagle 2020; Koposov et al. 2023a) to estimate the free parameters and their uncertainties. We used the following setup for all of our runs: `nlive_init=1000, dlogz_init=0.0001, nlive_batch=100,` and `maxbatch=100`[7].

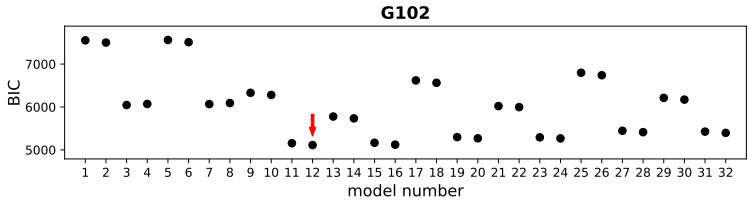

Figure 5.10: The Bayesian Information Criterion (BIC) for each model fitted to the G102 data. The model numbers are explained in Table 5.7. The red arrow marks the model with the lowest BIC.

[7]The various arguments are explained in `dynesty`'s documentation: `https://dynesty.readthedocs.io/en/latest/api.html\#dynesty.dynamicsampler.DynamicSampler.run_nested`

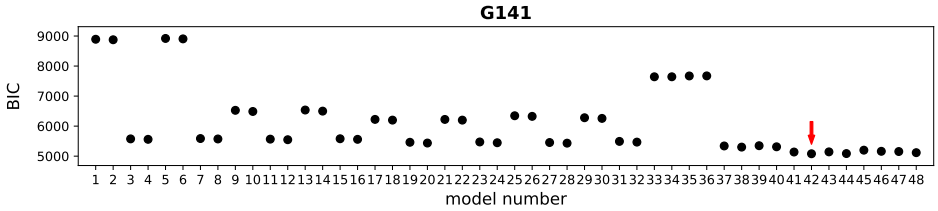

Figure 5.11: The Bayesian Information Criterion (BIC) for each model fitted to the G141 data. The model numbers are explained in Table 5.8. The red arrow marks the model with the lowest BIC.

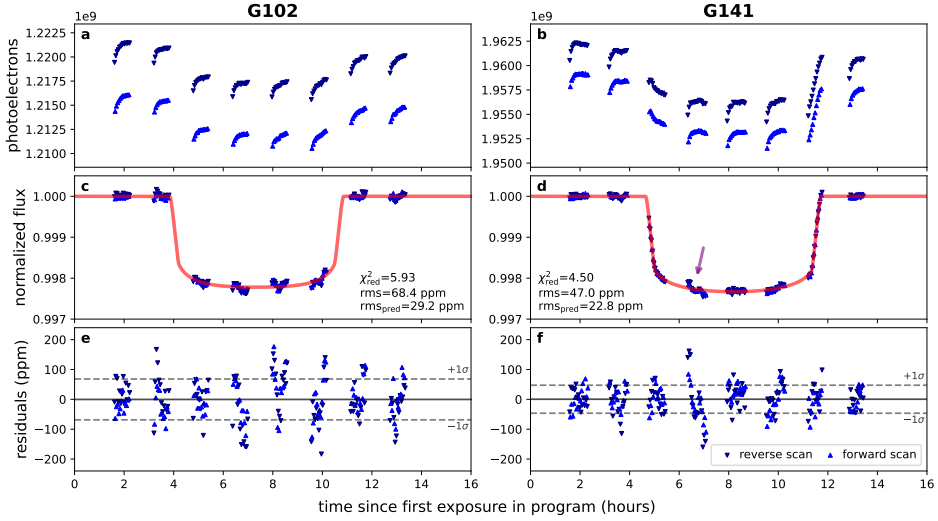

Figure 5.12: Best white light curve fits for the G102 and G141 observations when only removing the first orbit.

Table 5.7: All 32 white light curve fits run on the G102 dataset. The fit with the lowest Bayesian Information Criterion (BIC) is marked in bold. M_i: model number used in Figure 5.10, "visit model": function from Equation 5.3 used to model the visit-long systematics, "rem. orbits": lists which orbit was removed when performing the fit (e.g., "1,2" corresponds to the removal of the first and second orbit), LD: linear limb-darkening (1) or two parameter limb darkening (2) following Kipping (2013), "r_3": "Y" if the delay function was used in the fit, or "N" if not, "$N_{\mathrm{f.p.}}$": number of free parameters in the fit, rms (ppm): the root-mean-square of the residuals in parts-per-million (ppm), ×phot.: the factor by which the rms of the residuals is above the photon limit, χ^2: the chi-squared, $\chi^2_{\mathrm{red.}}$: the reduced chi-squared, BIC: the Bayesian Information Criterion, ΔBIC: the difference between the respective BIC (BIC_i) and the lowest BIC in the list ($\mathrm{BIC}_{\mathrm{min}}$) (so: $\Delta\mathrm{BIC} = \mathrm{BIC}_i - \mathrm{BIC}_{\mathrm{min}}$), and $\log \mathcal{Z}$ the final evidence outputted by `dynesty`. The predicted rms in the case of photon-noise-limited observations for G102 was 29.2 ppm.

M_i	visit model	rem. orbits	LD	r_3	$N_{\mathrm{f.p.}}$	rms (ppm)	×phot.	χ^2	$\chi^2_{\mathrm{red.}}$	BIC	ΔBIC	$\log \mathcal{Z}$	$\Delta \log \mathcal{Z}$
1	lin.	1	1	N	11	111.7	3.8	2936.9	15.54	7553.2	2441.6	-2700.9	-393.9
2	lin.	1	2	N	12	110.6	3.8	2879.8	15.32	7501.4	2389.8	-2699.9	-393.0
3	lin.	1,2	1	N	11	98.6	3.4	2000.4	12.20	6045.4	933.8	-2350.8	-43.9
4	lin.	1,2	2	N	12	99.0	3.4	2019.9	12.39	6070.2	958.5	-2349.9	-43.0
5	lin.	1	1	Y	12	111.8	3.8	2940.2	15.64	7561.8	2450.1	-2701.7	-394.7
6	lin.	1	2	Y	13	110.7	3.8	2883.5	15.42	7510.4	2398.7	-2702.4	-395.5
7	lin.	1,2	1	Y	12	99.0	3.4	2016.8	12.37	6067.1	955.4	-2355.9	-48.9
8	lin.	1,2	2	Y	13	99.5	3.4	2036.5	12.57	6091.9	980.3	-2353.9	-47.0
9	quad.	1	1	N	12	85.2	2.9	1708.8	9.09	6330.4	1218.7	-2658.8	-351.8
10	quad.	1	2	N	13	83.8	2.9	1653.6	8.84	6280.5	1168.9	-2658.3	-351.3
11	quad.	1,2	1	N	12	73.3	2.5	1105.7	6.78	5155.9	44.3	-2310.1	-3.2
12	**quad.**	**1,2**	**2**	**N**	**13**	**71.6**	**2.5**	**1056.3**	**6.52**	**5111.6**	**0.0**	**-2306.9**	**0.0**
13	quad.	1	1	Y	13	69.9	2.4	1150.2	6.15	5777.1	665.5	-2624.8	-317.8
14	quad.	1	2	Y	14	68.4	2.3	1102.1	5.93	5734.3	622.7	-2621.0	-314.0
15	quad.	1,2	1	Y	13	73.4	2.5	1110.2	6.85	5165.6	53.9	-2313.2	-6.3
16	quad.	1,2	2	Y	14	71.8	2.5	1061.0	6.59	5121.5	9.9	-2311.0	-4.0

Table 5.7: Continued.

17	exp.	1	1	N	12	92.2	3.2	1998.3	10.63	6619.9	1508.3	-2671.0	-364.1
18	exp.	1	2	N	13	90.7	3.1	1936.9	10.36	6563.8	1452.2	-2671.9	-364.9
19	exp.	1,2	1	N	12	77.8	2.7	1247.1	7.65	5297.3	185.6	-2317.7	-10.8
20	exp.	1,2	2	N	13	76.8	2.6	1213.8	7.49	5269.1	157.5	-2317.9	-10.9
21	exp.	1	1	Y	13	77.0	2.6	1394.4	7.46	6021.3	909.7	-2642.6	-335.6
22	exp.	1	2	Y	14	76.2	2.6	1364.9	7.34	5997.1	885.5	-2640.0	-333.1
23	exp.	1,2	1	Y	13	77.5	2.7	1236.2	7.63	5291.6	180.0	-2320.2	-13.2
24	exp.	1,2	2	Y	14	76.6	2.6	1207.0	7.50	5267.6	155.9	-2320.3	-13.4
25	log.	1	1	N	12	96.2	3.3	2176.5	11.58	6798.1	1686.5	-2681.0	-374.0
26	log.	1	2	N	13	94.8	3.2	2113.0	11.30	6739.9	1628.2	-2679.4	-372.4
27	log.	1,2	1	N	12	82.3	2.8	1395.7	8.56	5445.9	334.3	-2325.4	-18.5
28	log.	1,2	2	N	13	81.2	2.8	1357.5	8.38	5412.8	301.2	-2323.1	-16.2
29	log.	1	1	Y	13	82.1	2.8	1585.1	8.48	6212.1	1100.4	-2651.4	-344.5
30	log.	1	2	Y	14	80.9	2.8	1539.7	8.28	6171.9	1060.2	-2647.1	-340.2
31	log.	1,2	1	Y	13	81.6	2.8	1370.0	8.46	5425.4	313.7	-2324.6	-17.6
32	log.	1,2	2	Y	14	80.6	2.8	1336.0	8.30	5396.5	284.9	-2322.7	-15.8

Table 5.8: All 32 white light curve fits run on the G141 dataset. Parameters like in Table 5.7. The predicted rms in the case of photon-noise-limited observations for G141 was 22.8 ppm.

M_i	visit model	rem. orbits	LD	r_3	$N_{\mathrm{f.p.}}$	rms (ppm)	×phot.	χ^2	$\chi^2_{\mathrm{red.}}$	BIC	ΔBIC	$\log \mathcal{Z}$	$\Delta \log \mathcal{Z}$
1	lin.	1	1	N	11	92.3	4.0	3647.8	17.21	8892.4	3812.4	-3073.4	-557.0
2	lin.	1	2	N	12	92.0	4.0	3625.9	17.19	8875.9	3795.9	-3074.4	-558.0

Table 5.8: Continued.

3	lin.	1,2	1	N	11	52.7	2.3	1030.1	5.66	5575.4	495.5	-2564.0	-47.6
4	lin.	1,2	2	N	12	52.2	2.3	1009.7	5.58	5560.3	480.4	-2565.5	-49.1
5	lin.	1	1	Y	12	92.5	4.1	3669.5	17.39	8919.4	3839.4	-3078.8	-562.4
6	lin.	1	2	Y	13	92.3	4.0	3649.9	17.38	8905.3	3825.3	-3078.8	-562.4
7	lin.	1,2	1	Y	12	52.9	2.3	1036.1	5.72	5586.7	506.8	-2569.7	-53.3
8	lin.	1,2	2	Y	13	52.4	2.3	1016.9	5.65	5572.8	492.8	-2569.4	-53.0
9	quad.	1	1	N	12	54.6	2.4	1276.4	6.05	6526.3	1446.4	-2972.9	-456.5
10	quad.	1	2	N	13	53.7	2.4	1232.7	5.87	6488.1	1408.1	-2970.2	-453.8
11	quad.	1,2	1	N	12	52.4	2.3	1016.1	5.61	5566.8	486.8	-2570.5	-54.1
12	quad.	1,2	2	N	13	51.7	2.3	991.9	5.51	5547.8	467.8	-2572.5	-56.1
13	quad.	1	1	Y	13	54.7	2.4	1280.8	6.10	6536.2	1456.2	-2976.4	-460.0
14	quad.	1	2	Y	14	53.8	2.4	1238.6	5.93	6499.4	1419.4	-2972.9	-456.5
15	quad.	1,2	1	Y	13	52.6	2.3	1023.9	5.69	5579.8	499.8	-2577.8	-61.4
16	quad.	1,2	2	Y	14	51.9	2.3	999.2	5.58	5560.4	480.4	-2577.4	-61.0
17	exp.	1	1	N	12	47.7	2.1	974.2	4.62	6224.2	1144.2	-2942.9	-426.5
18	exp.	1	2	N	13	47.0	2.1	944.8	4.50	6200.1	1120.1	-2941.5	-425.1
19	exp.	1,2	1	N	12	49.6	2.2	911.5	5.04	5462.1	382.1	-2560.6	-44.2
20	exp.	1,2	2	N	13	48.8	2.1	881.0	4.89	5436.9	356.9	-2559.8	-43.4
21	exp.	1	1	Y	13	47.5	2.1	967.8	4.61	6223.1	1143.1	-2947.5	-431.1
22	exp.	1	2	Y	14	46.8	2.1	939.1	4.49	6199.9	1119.9	-2941.9	-425.5
23	exp.	1,2	1	Y	13	49.8	2.2	916.8	5.09	5472.7	392.7	-2565.7	-49.3
24	exp.	1,2	2	Y	14	48.9	2.1	885.8	4.95	5447.0	367.0	-2564.0	-47.6
25	log.	1	1	N	12	50.6	2.2	1095.6	5.19	6345.5	1265.6	-2953.6	-437.2
26	log.	1	2	N	13	50.0	2.2	1069.9	5.10	6325.3	1245.3	-2953.6	-437.2

Table 5.8: Continued.

27	log.	1,2	1	N	12	49.4	2.2	903.7	4.99	5454.3	374.3	-2557.6	-41.2
28	log.	1,2	2	N	13	48.7	2.1	877.0	4.87	5432.9	352.9	-2557.6	-41.2
29	log.	1	1	Y	13	48.9	2.1	1024.1	4.88	6279.5	1199.5	-2945.1	-428.7
30	log.	1	2	Y	14	48.3	2.1	996.8	4.77	6257.6	1177.6	-2942.8	-426.4
31	log.	1,2	1	Y	13	50.3	2.2	935.7	5.20	5491.6	411.7	-2560.5	-44.1
32	log.	1,2	2	Y	14	49.5	2.2	906.7	5.07	5467.8	387.8	-2559.2	-42.8
33	lin.	1,5	1	N	11	91.4	4.0	3097.6	17.02	7643.0	2563.0	-2666.2	-149.8
34	lin.	1,5	2	N	12	91.3	4.0	3092.6	17.09	7643.3	2563.3	-2667.8	-151.4
35	lin.	1,5	1	Y	12	91.7	4.0	3119.9	17.24	7670.6	2590.7	-2670.1	-153.7
36	lin.	1,5	2	Y	13	91.7	4.0	3116.8	17.32	7672.8	2592.8	-2671.8	-155.4
37	quad.	1,5	1	N	12	46.1	2.0	789.0	4.36	5339.7	259.7	-2551.2	-34.8
38	quad.	1,5	2	N	12	45.0	2.0	750.6	4.15	5301.4	221.4	-2546.9	-30.5
39	quad.	1,5	1	Y	13	46.2	2.0	792.2	4.40	5348.2	268.2	-2555.6	-39.2
40	quad.	1,5	2	Y	14	45.0	2.0	750.8	4.20	5312.1	232.1	-2551.6	-35.2
41	exp.	1,5	1	N	12	39.8	1.7	586.9	3.24	5137.7	57.7	-2525.5	-9.1
42	**exp.**	**1,5**	**2**	**N**	**13**	**37.6**	**1.6**	**524.0**	**2.91**	**5080.0**	**0.0**	**-2516.4**	**0.0**
43	exp.	1,5	1	Y	13	39.8	1.7	586.9	3.26	5142.9	62.9	-2527.0	-10.6
44	exp.	1,5	2	Y	14	37.6	1.6	525.4	2.94	5086.6	6.7	-2517.7	-1.3
45	log.	1,5	1	N	12	41.8	1.8	648.7	3.58	5199.4	119.5	-2531.5	-15.1
46	log.	1,5	2	N	13	40.4	1.8	605.8	3.37	5161.7	81.8	-2525.7	-9.3
47	log.	1,5	1	Y	13	40.2	1.8	598.3	3.32	5154.3	74.3	-2522.6	-6.2
48	log.	1,5	2	Y	14	38.7	1.7	555.3	3.10	5116.5	36.5	-2517.9	-1.5

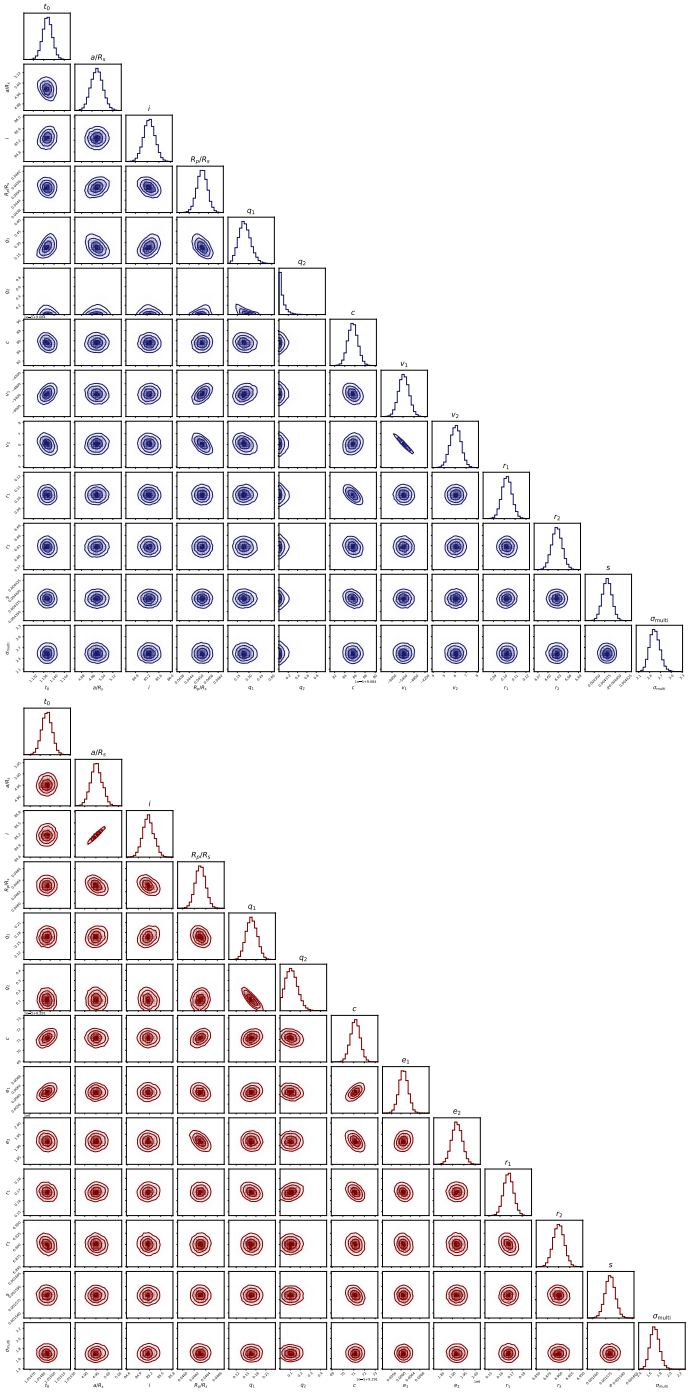

Figure 5.13: Corner plots for the white light curve fits based on the G102 and G141 data sets on the left and right sides, respectively.

5.B Spectroscopic light curve fits

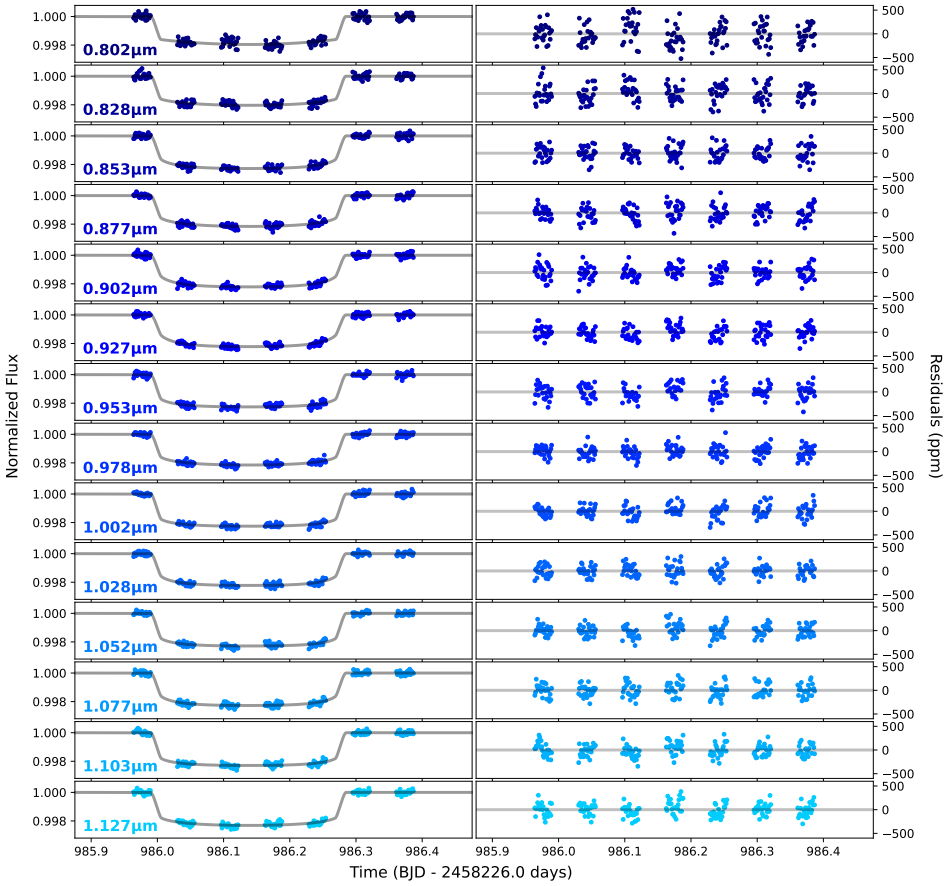

Figure 5.14: All spectroscopic light curve fits for the G102 data. The left column shows the best-fitting transit model to the light curve with the systematics removed. The right column shows the residuals of our best light curve fit.

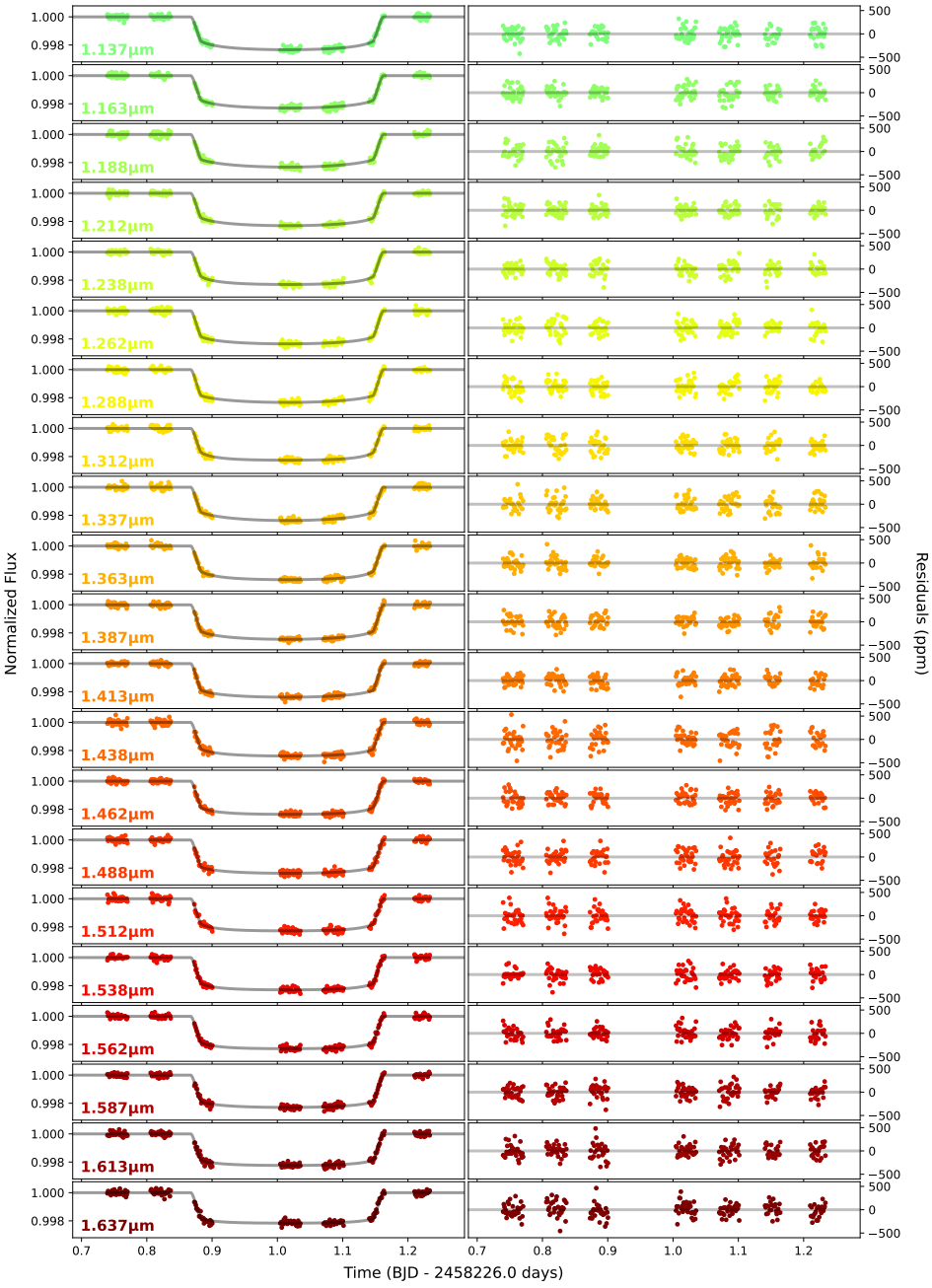

Figure 5.15: Same as Figure 5.14 but for the G141 data.

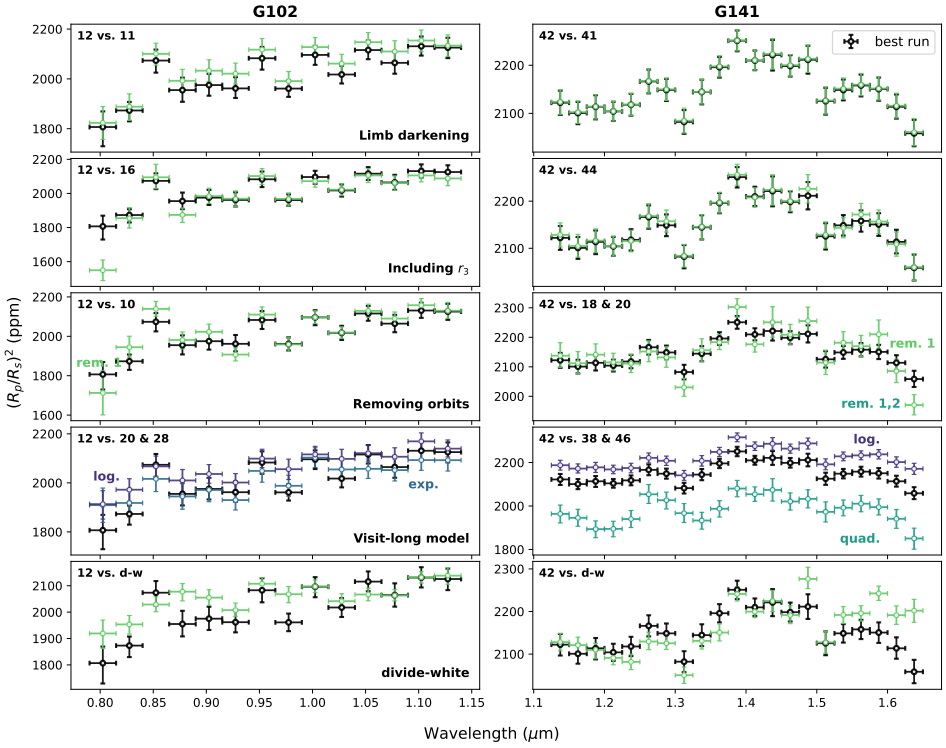

Figure 5.16: Plot showing how different model assumptions change the transmission spectrum for the G102 data (left column) and for the G141 data (right column). The top left of each subplot lists the specific models shown following the model number M_i in Table 5.7 (for G102) and Table 5.8 (for G141). The last row compares our best run (black), with a `divide-white` run. The transit depth remains fairly flat on the red edge for the `divide-white` G141 transmission spectrum, like in Colón et al. (2020) (see Fig. 5.7).

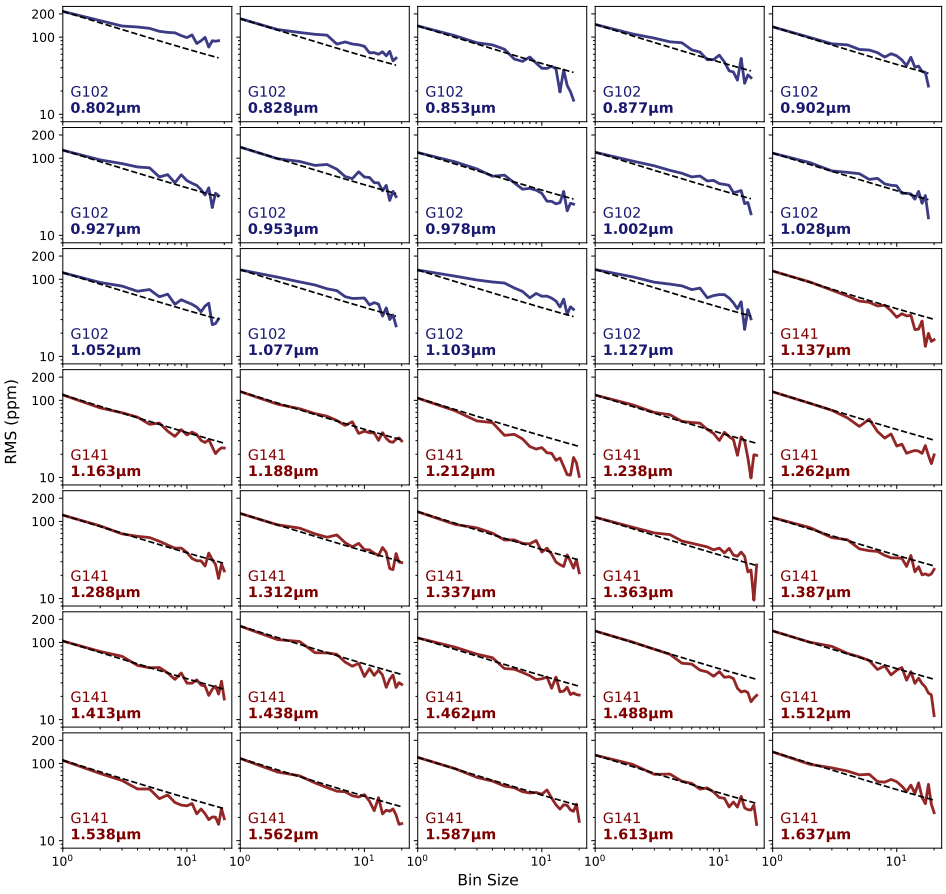

Figure 5.17: Allan deviation plots for all spectroscopic light curve fits.

Table 5.9: Various properties of the spectroscopic light curve fits. The predicted rms in the case of photon-noise-limited observations is $\mathrm{rms}_{\mathrm{pred.}}$. σ_{multi} is the uncertainty-multiplier factor described in Section 5.3.1. Other parameters (rms, ×phot., χ^2, and $\chi^2_{\mathrm{red.}}$) are explained in Table 5.7. q_1 and q_2 are the parameters of the quadratic limb darkening law following the Kipping (2013) parameterization. We used q_1 and q_2 to derive the two parameters u_1 and u_2 from the popular quadratic limb darkening law.

λ_{mid} (µm)	rms	$\mathrm{rms}_{\mathrm{pred.}}$	×phot .	χ^2	$\chi^2_{\mathrm{red.}}$	σ_{multi}	q_1	q_2	u_1	u_2
G102										
0.802	215.4	190.2	1.13	224	1.36	1.27	$0.06^{+0.05}_{-0.03}$	$0.89^{+0.08}_{-0.14}$	$0.39^{+0.10}_{-0.12}$	$-0.17^{+0.06}_{-0.05}$
0.828	173.3	153.7	1.13	223	1.35	1.26	$0.11^{+0.07}_{-0.06}$	$0.42^{+0.21}_{-0.21}$	$0.27^{+0.09}_{-0.10}$	$0.05^{+0.18}_{-0.12}$
0.853	139.7	135.2	1.03	187	1.13	1.06	$0.26^{+0.11}_{-0.09}$	$0.12^{+0.18}_{-0.08}$	$0.12^{+0.13}_{-0.08}$	$0.39^{+0.16}_{-0.22}$
0.877	146.1	123.7	1.18	244	1.48	1.24	$0.21^{+0.10}_{-0.09}$	$0.26^{+0.23}_{-0.16}$	$0.23^{+0.11}_{-0.13}$	$0.21^{+0.22}_{-0.21}$
0.902	135.9	113.5	1.20	251	1.52	1.24	$0.38^{+0.16}_{-0.14}$	$0.09^{+0.11}_{-0.06}$	$0.11^{+0.09}_{-0.07}$	$0.50^{+0.18}_{-0.21}$
0.927	126.9	108.0	1.17	242	1.46	1.23	$0.45^{+0.13}_{-0.14}$	$0.07^{+0.11}_{-0.05}$	$0.09^{+0.11}_{-0.07}$	$0.58^{+0.14}_{-0.22}$
0.953	139.1	104.1	1.34	312	1.89	1.36	$0.20^{+0.08}_{-0.07}$	$0.10^{+0.12}_{-0.07}$	$0.08^{+0.08}_{-0.06}$	$0.35^{+0.12}_{-0.15}$
0.978	118.3	100.9	1.17	241	1.46	1.20	$0.20^{+0.13}_{-0.09}$	$0.21^{+0.27}_{-0.16}$	$0.19^{+0.12}_{-0.13}$	$0.25^{+0.24}_{-0.24}$
1.002	119.4	99.3	1.20	253	1.53	1.24	$0.15^{+0.07}_{-0.07}$	$0.11^{+0.18}_{-0.08}$	$0.09^{+0.09}_{-0.06}$	$0.30^{+0.12}_{-0.18}$
1.028	116.3	98.0	1.19	246	1.49	1.23	$0.29^{+0.10}_{-0.10}$	$0.06^{+0.12}_{-0.05}$	$0.07^{+0.09}_{-0.05}$	$0.47^{+0.12}_{-0.19}$
1.052	121.7	98.6	1.23	267	1.61	1.28	$0.18^{+0.08}_{-0.07}$	$0.08^{+0.14}_{-0.06}$	$0.07^{+0.09}_{-0.05}$	$0.35^{+0.12}_{-0.16}$
1.077	132.5	99.3	1.33	311	1.89	1.38	$0.28^{+0.10}_{-0.10}$	$0.07^{+0.12}_{-0.05}$	$0.08^{+0.09}_{-0.06}$	$0.46^{+0.12}_{-0.19}$
1.103	131.5	101.4	1.30	294	1.78	1.33	$0.15^{+0.09}_{-0.07}$	$0.11^{+0.18}_{-0.08}$	$0.09^{+0.09}_{-0.06}$	$0.30^{+0.15}_{-0.18}$
1.127	133.6	103.8	1.29	290	1.76	1.37	$0.15^{+0.12}_{-0.09}$	$0.27^{+0.47}_{-0.20}$	$0.21^{+0.14}_{-0.14}$	$0.18^{+0.27}_{-0.29}$
G141										
1.137	127.8	115.5	1.11	236	1.29	1.14	$0.19^{+0.04}_{-0.03}$	$0.26^{+0.17}_{-0.14}$	$0.23^{+0.12}_{-0.12}$	$0.21^{+0.15}_{-0.15}$
1.163	117.6	113.1	1.04	209	1.14	1.07	$0.16^{+0.03}_{-0.03}$	$0.31^{+0.18}_{-0.15}$	$0.25^{+0.11}_{-0.11}$	$0.15^{+0.14}_{-0.14}$

Table 5.9: Continued.

1.188	129.8	109.6	1.18	271	1.48	1.22	$0.13^{+0.03}_{-0.03}$	$0.46^{+0.22}_{-0.19}$	$0.34^{+0.11}_{-0.13}$	$0.03^{+0.16}_{-0.14}$
1.212	106.8	107.5	0.99	190	1.04	1.02	$0.16^{+0.03}_{-0.03}$	$0.31^{+0.16}_{-0.14}$	$0.25^{+0.10}_{-0.11}$	$0.15^{+0.14}_{-0.13}$
1.238	117.1	105.9	1.11	236	1.29	1.14	$0.19^{+0.03}_{-0.03}$	$0.15^{+0.14}_{-0.10}$	$0.13^{+0.10}_{-0.08}$	$0.30^{+0.11}_{-0.13}$
1.262	129.0	105.9	1.22	286	1.56	1.25	$0.13^{+0.03}_{-0.03}$	$0.30^{+0.20}_{-0.16}$	$0.22^{+0.12}_{-0.11}$	$0.15^{+0.14}_{-0.15}$
1.288	120.6	105.2	1.15	254	1.39	1.18	$0.11^{+0.03}_{-0.02}$	$0.43^{+0.23}_{-0.19}$	$0.28^{+0.11}_{-0.12}$	$0.05^{+0.15}_{-0.14}$
1.312	126.8	104.0	1.22	287	1.57	1.25	$0.20^{+0.03}_{-0.03}$	$0.07^{+0.09}_{-0.05}$	$0.06^{+0.08}_{-0.05}$	$0.39^{+0.06}_{-0.10}$
1.337	133.3	103.8	1.28	318	1.74	1.32	$0.16^{+0.03}_{-0.03}$	$0.43^{+0.20}_{-0.18}$	$0.34^{+0.12}_{-0.12}$	$0.05^{+0.15}_{-0.15}$
1.363	113.3	104.1	1.09	229	1.25	1.12	$0.19^{+0.03}_{-0.03}$	$0.17^{+0.13}_{-0.10}$	$0.15^{+0.10}_{-0.09}$	$0.29^{+0.11}_{-0.12}$
1.387	112.0	105.8	1.06	216	1.18	1.09	$0.15^{+0.03}_{-0.03}$	$0.31^{+0.17}_{-0.14}$	$0.24^{+0.10}_{-0.10}$	$0.15^{+0.13}_{-0.13}$
1.413	104.4	106.3	0.98	186	1.02	1.01	$0.12^{+0.02}_{-0.02}$	$0.31^{+0.17}_{-0.15}$	$0.21^{+0.10}_{-0.10}$	$0.13^{+0.12}_{-0.12}$
1.438	162.7	107.6	1.51	442	2.41	1.56	$0.13^{+0.03}_{-0.03}$	$0.20^{+0.21}_{-0.14}$	$0.15^{+0.13}_{-0.10}$	$0.22^{+0.12}_{-0.16}$
1.462	114.5	108.1	1.06	217	1.19	1.09	$0.15^{+0.02}_{-0.02}$	$0.09^{+0.11}_{-0.06}$	$0.07^{+0.08}_{-0.05}$	$0.32^{+0.06}_{-0.09}$
1.488	140.7	110.2	1.28	315	1.72	1.31	$0.10^{+0.03}_{-0.03}$	$0.26^{+0.24}_{-0.17}$	$0.17^{+0.12}_{-0.11}$	$0.15^{+0.13}_{-0.15}$
1.512	141.1	111.3	1.27	310	1.69	1.30	$0.16^{+0.03}_{-0.03}$	$0.09^{+0.12}_{-0.06}$	$0.07^{+0.08}_{-0.05}$	$0.32^{+0.07}_{-0.11}$
1.538	109.9	112.2	0.98	185	1.01	1.01	$0.14^{+0.02}_{-0.02}$	$0.09^{+0.10}_{-0.06}$	$0.06^{+0.07}_{-0.05}$	$0.30^{+0.06}_{-0.09}$
1.562	116.3	115.0	1.01	198	1.08	1.04	$0.13^{+0.02}_{-0.02}$	$0.08^{+0.11}_{-0.06}$	$0.06^{+0.07}_{-0.04}$	$0.30^{+0.06}_{-0.09}$
1.587	120.2	117.8	1.02	201	1.10	1.05	$0.09^{+0.02}_{-0.02}$	$0.28^{+0.23}_{-0.16}$	$0.17^{+0.11}_{-0.10}$	$0.14^{+0.12}_{-0.14}$
1.613	128.6	119.7	1.07	223	1.22	1.10	$0.10^{+0.02}_{-0.02}$	$0.14^{+0.17}_{-0.10}$	$0.09^{+0.09}_{-0.06}$	$0.23^{+0.08}_{-0.11}$
1.637	141.6	123.3	1.15	255	1.39	1.18	$0.08^{+0.02}_{-0.02}$	$0.07^{+0.10}_{-0.05}$	$0.04^{+0.05}_{-0.03}$	$0.25^{+0.05}_{-0.07}$